

# **On the two-dimensional structure of short gravity waves in a wind wave tank**

Andrey Zavadsky, Alvise Benetazzo, and Lev Shemer

Citation: [Phys. Fluids](#) **29**, 016601 (2017); doi: 10.1063/1.4973319

View online: <http://dx.doi.org/10.1063/1.4973319>

View Table of Contents: <http://aip.scitation.org/toc/phf/29/1>

Published by the [American Institute of Physics](#)

---

---



# On the two-dimensional structure of short gravity waves in a wind wave tank

Andrey Zavadsky,<sup>1</sup> Alvise Benetazzo,<sup>2</sup> and Lev Shemer<sup>1,a)</sup>

<sup>1</sup>School of Mechanical Engineering, Tel-Aviv University, Tel-Aviv, Israel

<sup>2</sup>CNR-ISMAR, Institute of Marine Sciences, National Research Council, Arsenale-Tesa 104, Castello 2737/F, I-30122 Venice, Italy

(Received 26 September 2016; accepted 12 December 2016; published online 6 January 2017)

Experiments on wind-waves in a laboratory tank are carried out for a variety of operational conditions. In addition to using a conventional wave gauge to determine the temporal variation of the surface elevation at the sensor location, independent measuring techniques such as 3D reconstruction of stereo video images and 2D laser slope gauge are applied in order to gain information on the three-dimensional structure of the wind-wave field. The consistency of results obtained by different methods under identical forcing conditions is examined to establish the limits of applicability and accuracy of each method. The accumulated results on the spatial and temporal coherence of the surface elevation variation, on the directional wave spectra, and on the probability distribution of the instantaneous surface slope directions demonstrate that the wind-wave field is essentially three-dimensional and short-crested. *Published by AIP Publishing.* [<http://dx.doi.org/10.1063/1.4973319>]

## I. INTRODUCTION

Wind-generated sea waves affect a wide range of activities such as ship navigation, offshore industry, coastal environment, and pollution control. Spatial and temporal variabilities of wind forcing coupled with the unsteadiness and inhomogeneity of wind waves in the ocean make quantitative field measurements extremely challenging, so that results gained in field experiments are characterized by considerable scatter. Accurate experiments are therefore needed for better understanding of the behavior of wind-waves under different conditions and for validation of theoretical models.

Although experiments performed under controlled conditions offer clear advantages over field measurements, waves excited in any laboratory tank apparently are very different from those in the ocean. Wavelengths even in the largest available facilities are shorter by orders of magnitude than the lengths of typical sea waves. Ocean waves exhibit considerable angular spreading, whereas in wind-wave tanks the deviation of the waves from the downwind direction as well as possible effects of side walls often does not attract sufficient attention. Young wind waves in laboratory are usually steeper than those in ocean resulting in stronger nonlinearity. Moreover, the frequency of relatively short waves in laboratory is affected by wind-induced shear current, preventing the straightforward application of the linear dispersion relation for gravity-capillary waves for the determination of the wavelength from the measured wave frequency. Wind-waves in laboratory may contain considerable energy at frequencies and wavelengths where the effects of capillarity become essential. Due to these and additional differences between water-waves in laboratory and in nature, the relevance of

small-scale experiments to full-scale phenomena is sometimes questioned.

To address the issue of different scales, data obtained in field experiments should be compared with the laboratory results using an appropriate scaling. Zavadsky *et al.*<sup>1</sup> performed detailed measurements of the surface elevation variation with time for a range of wind velocities and fetches. They determined variation of governing parameters of the wave field, such as the peak wave frequency  $f_p$  and the Root Mean Square (RMS) value of the surface elevation,  $\langle \eta^2 \rangle^{1/2}$ , on the fetch  $x$ . When rendered dimensionless, these dependencies did not differ notably from those obtained in laboratory by Mitsuyasu<sup>2</sup> and Mitsuyasu and Honda,<sup>3</sup> and from the results of field experiments.<sup>4–6</sup>

Zavadsky *et al.*<sup>1</sup> also demonstrated that the wave power spectrum measured at different fetches and wind velocities, when properly normalized, collapses on a single appropriately normalized JONSWAP spectral shape. The similarity of wave spectra measured in laboratory to the standard JONSWAP shape that is based on extensive measurements in the North Sea<sup>4</sup> was noticed already by Plant.<sup>7</sup> These results on wind waves evolving under steady forcing demonstrate that with suitable scaling conclusions based on small-scale experiments may be applicable for phenomena at much larger scales.

Experiments on waves in general and on wind-generated waves, in particular, are mostly based on measurements by wave gauges that provide information on the temporal variation of the surface elevation at the sensor location. Diverse approaches were applied in attempts to extract information on the spatial structure of the wave field. Linear arrays of point sensors such as used by Mitsuyasu *et al.*<sup>8</sup> and Wang and Hwang,<sup>9</sup> among others, are able to provide partial spatial information on the wave field, since the length of the array and the spacing of the wire gages impose the limitations of the wavelength that can be measured. Application of a 2D array of

<sup>a)</sup>Author to whom correspondence should be addressed. Electronic mail: shemer@eng.tau.ac.il

sensors provides a possibility to estimate directional spreading of waves.<sup>10</sup>

A wide variety of nonintrusive optical methods has been applied to study water waves in the recent decades; these methods often are capable of providing data on the spatial structure of an individual wave or of the wave field. A laser sheet projected on the water surface allows one to obtain one-dimensional spatial measurements of the wave profile.<sup>11,12</sup> Laser slope-gauge (LSG) is a frequently used optical instrument with very fast response; it provides information on the one- or two-dimensional surface slope by measuring the position of a laser beam refracted by the water surface waves.<sup>13–16</sup> The sensitivity of LSG to the surface slope rather than to the elevation makes it advantageous for the investigation of ripples.<sup>17–20</sup> Barter *et al.*<sup>21</sup> and Donelan and Plant<sup>22</sup> used modifications of the LSG technique that allowed measuring simultaneously the surface elevation and slope. A scanning version of the laser slope-gauge (SLSG) enables obtaining wavenumber-frequency spectra of very short waves.<sup>23–26</sup>

First attempts to obtain quantitative data on an extensive area of the ocean were made by Cox and Munk<sup>27</sup> who exploited the reflection of sun light from the water surface to retrieve statistical information on the slope distribution. More recently, advances in digital imaging and processing accelerated development of various methods that enable the 3D reconstruction of the water surface.<sup>28–34</sup> Some of the implementations of this approach allow simultaneous measurements of both the wave slope and the surface elevation.<sup>35</sup> All those methods require a careful arrangement of illumination and thus are used exclusively in laboratory over relatively small areas; their application in field experiments is impractical.

It is natural to attempt to apply stereo imaging to obtain the spatial distribution of the water surface elevation. Early attempts in this direction used two synchronized photo cameras located above the water surface with a known spatial separation. The overlapping parts of the images are analyzed to obtain the surface height distribution. Cote *et al.*<sup>36</sup> used two airborne cameras to estimate the directional wave vector spectrum. Shemdin *et al.*<sup>37</sup> and Banner *et al.*<sup>38</sup> were among the first to apply stereo imaging to analyze quantitatively the spectral characteristics of short gravity waves. Wanek and Wu<sup>39</sup> developed a trinocular stereo imaging system demonstrating excellent agreement with the results obtained by the standard wave gauge measurements.

Owing to increasing computational power and development of more effective algorithms, stereo video imaging replaced photography during the last decade.<sup>40–46</sup> So far, the stereo video imaging was used in field experiments with cameras installed either on offshore platforms or on a moving vessel. Comparison of video imaging results with those obtained using a standard instrumentation that was carried out in those experiments provided evidence that at open sea scales, stereo wave imaging is effective to retrieve medium-to-short wavelengths.

Stereo video imaging, similarly to alternative methods of reconstruction of the instantaneous water surface shape, requires considerable computational resources that currently limit their effective spatial resolution and the overall duration of continuous imaging. Contrary to other methods, however,

the stereo video imaging of the sea surface may use natural illumination and is capable of covering areas of the order of  $100 \text{ m}^2$ . The question of accuracy of the surface shape obtained using stereo imaging, however, has not yet been satisfactorily resolved. Due to growing number of field experiments based on this method, it is essential to obtain independent estimates of the accuracy and of the limitations of this technique.

In the present study, we apply stereo video imaging in a small-scale wind-wave flume to study the two-dimensional structure of the wind-wave field under controlled conditions. Fast video recording enables extracting both the temporal and spatial information. Information on the spatially evolving under steady wind forcing wave field in the tank is also obtained using a conventional capacitance-type wave gauge as well as a laser slope gauge. Application of optical methods allows augmenting the wave gauge data by providing data on the wave directional spreading. Measurements performed under different wind forcing conditions enable the accumulation of large ensembles of data at several fetches. The experiments therefore cover a range of periods and lengths of the dominant waves. Application of various instruments under identical forcing conditions enables the verification of reliability and determination of the limitations of the applied methods.

## II. EXPERIMENTAL FACILITY, CALIBRATION, AND DATA ACQUISITION

### A. The wind-wave flume

Experiments were performed in a small-scale wind-wave flume shown schematically in Fig. 1. The system consists of a closed-loop wind tunnel over a 5 m long test section with the cross section  $0.4 \times 0.5 \text{ m}^2$ . Sidewalls and the bottom of the test section are made of clear glass to enable flow visualization of the wave field and application of optical measuring techniques from all directions. The test section is covered by transparent removable Perspex plates with a partially sealed slot along the centerline to facilitate positioning of the sensors. Water depth in the test section is about 0.2 m, satisfying deep-water conditions for wind-wave lengths pertinent to this study. A computer-controlled blower enables maximum wind speed in

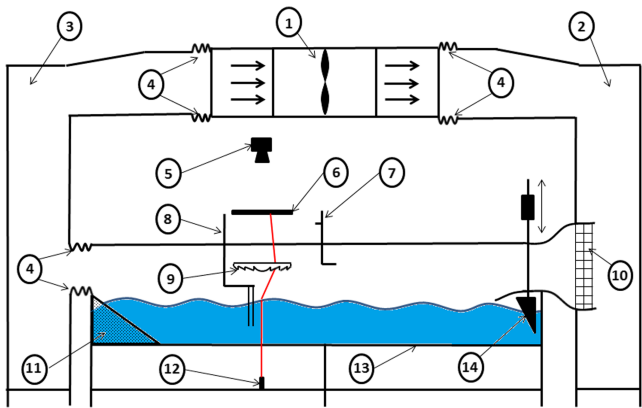


FIG. 1. Wind-wave flume scheme: 1 blower; 2 inflow settling chamber; 3 outflow settling chamber; 4 flexible connection; 5 PSD; 6 screen; 7 pitot tube driven by the stepper motor; 8 wave gauge driven by the stepper motor; 9 Fresnel lens; 10 contraction with honeycomb; 11 beach; 12 laser; 13 test section; 14 wavemaker driven by the servo-motor.

the test section that may exceed 15 m/s. A capacitance-type wave gauge made of 0.3 mm tantalum wires measures the instantaneous surface elevation  $\eta$ ; local mean air velocity is measured by a 3 mm pitot tube. The sensors are mounted on a carriage that can be moved to a desired fetch along the test section. The vertical position of the wave gauge is determined by a computer-controlled vertical stage to enable its static calibration. The pitot tube is mounted on a separate vertical stage and may be positioned at any height above the water surface. The wedge-type wave maker installed in the system is driven by a controlled Linear Motor P01-37X120. The wedge is installed beneath the entrance flap and is connected to the motor by thin vertical rods, thus introducing only a minor disturbance to the airflow. The intelligent servo controller E1100-GP that connects between the PC and the linear motor allows prescribing any desired pattern of the wave-maker motion. The blower and the wavemaker as well as the vertical positioning of the sensor and its calibration are controlled by a LabView program. The same program also performs the data acquisition. More details about the flume, the wave gauge calibration and measuring procedures are given in Liberzon and Shemer.<sup>47</sup>

## B. The laser slope gauge (LSG) assembly

The LSG measures simultaneously two components of the instantaneous surface slope without disturbing the water surface, thus providing information on the angular distribution of wind-generated waves. It is installed on a frame detached from the flume and can be positioned at any location along the tank. The instrument consists of four main parts: a laser diode, Fresnel lens, diffusive screen, and position-sensing detector (PSD) assembly, see Figure 1. The laser diode generates a 650 nm (red), 200 mW focusable laser beam with a diameter of about 0.5 mm. The smallest wavelength the instrument can resolve is estimated at approximately 2 mm. The 10.4 in. diameter Fresnel lens that has the focal length of 9 in. directs the incoming laser beam to the  $25 \times 25 \text{ cm}^2$  diffusive screen located in the back focal plane of the lens. The transmission coefficient of the lens is about 92%. The Fresnel lens and the diffusive screen are leveled horizontally and coaxially aligned with respect to their optical axes. The horizontal coordinates of the center of the laser beam spot on the screen that depend solely on the instantaneous surface slope and are independent of the surface elevation,<sup>48</sup> are recorded using position sensor detector PDP90A. The objective lens of the PSD with a focal length of 25 mm forms the image of the laser light spot on the diffusive screen at the sensor plane. The outputs of the two-dimensional, tetra-lateral PSD are related to the coordinates of this spot and translated into the values of the instantaneous surface slope components,  $\partial\eta/\partial x$  and  $\partial\eta/\partial y$ . The LSG system was calibrated using a number of optical prisms redirecting a laser beam by a known angle, ranging from  $2.5^\circ$  to  $17.5^\circ$ ; at each angle, the calibration was performed for a number of azimuthal positions of the beam. At each azimuthal angle, the response of PSD sensor was linear over the whole range of radial positions of the beam. More details on the LSG system and on the calibration procedure are given in Ref. 49. In order to measure the surface elevation  $\eta$  as well as both slope components, the wave gauge was mounted at the same fetch close to the laser slope gauge measuring location.

Measurements were performed at three distances from the test section inlet (fetches):  $x = 110 \text{ cm}$ ,  $x = 220 \text{ cm}$ , and  $x = 340 \text{ cm}$ . At each fetch, measurements were performed for five values of the steady maximum wind velocity in the tank  $U$  ranging from 6.5 m/s to 10.5 m/s. Zavadsky and Shemer<sup>50</sup> carried out detailed measurements of airflow above wind-waves. These measurements carried out in the present facility for the same range of wind velocities yielded values of friction velocities  $u^*$  that range from 0.35 m/s to 0.85 m/s. The friction velocities in air grow with  $U$  but depend only weakly on the fetch. At each fetch and wind velocity, continuous records of the instantaneous surface elevation  $\eta$  and of the slope components  $\partial\eta/\partial x$  and  $\partial\eta/\partial y$  were acquired at a sampling rate of 300 Hz; the total sampling duration exceeded 3 h.

## C. Stereo wave imaging

For stereo imaging of the wind-wave field, the sensors were removed, and the video images were acquired, in a separate set of experiments, at three fetches and three wind speeds. The stereo-camera system consists of two adjacent CMOS cameras (VIEWORKS VC-4MC, with 2048 columns by 2048 rows array of  $5.5 \mu\text{m}$  square active elements) mounting low-distortion 12 mm-focal length lenses, and placed side-by-side with a fixed baseline (i.e., the distance between the camera principal points) of 0.07 m, so that the two optical axes are parallel. Cameras were installed along the side window of the test section at a distance of about 1 m from the along-channel axis and tilted at  $50^\circ$  from the horizontal plane. The trigger input of each camera allows precise synchronization; the system is capable of providing 4 Mb images at the rate up to 180 fps. Care was taken to keep both cameras equidistant from the tank wall. Uniform pulsed illumination of the wind-wave field is provided by two 14 in.  $\times$  14 in. white LED panels. The panels that operate in a stroboscopic mode were mounted above the imaged location replacing the Perspex roof of the test section. To avoid uncontrolled reflections, a white background sheet was attached to the wall opposite to the cameras; a black rubber sheet was put on the bottom of the channel. The cameras and the LED panels were synchronized via the digital video recording (DVR) system capable of transferring data at the rate of 1.4 Gb/s. To calibrate the parameters of each camera (i.e., internal parameters) and the stereo-camera pose (i.e., external parameters), a MATLAB® calibration toolbox was used.<sup>51</sup>

The calibration procedure is carried out in two steps. First, the internal parameters (camera principal point, focal length, and lens distortion parameters) are determined for each camera using a specific planar target (i.e., a chessboard). Second, external parameters describing the rigid motion between the cameras (subject to 6 degrees of freedom) are recovered. The calibration quality was quantified by the reprojection error in the determination of the chessboard corners. During our tests, the errors were zero on average and did not exceed 0.4 pixels. The complete set of calibration parameters was obtained before each experimental run by repeating the entire procedure. In general, as both cameras were firmly fixed on a common support and lenses were left mounted on the cameras, no sensible changes between the runs occurred. Finally, after the calibration and before the stereo processing, each image pair is stereo

rectified to allow a fast epipolar search of corresponding image features along pixel rows. At each fetch and wind velocity, stereo images were acquired at a frame rate of 100 fps at full resolution ( $2048 \times 2048$  pixels) for 2 min. The stereo-matching algorithm developed by Benetazzo *et al.*<sup>41</sup> was used for the reconstruction of 3D water surface elevation distributions. Since the reconstruction procedure is time-consuming, each fifth frame of every sequence was usually processed to reduce the computational time. The clouds of 3D points resulting from the stereo process were bilinearly interpolated on a regular horizontal grid with a uniform spatial resolution of 1 mm. Thus, 21 600 pairs with a captured common imaged area of  $0.25 \text{ m} \times 0.40 \text{ m}$  were processed using a parallel cluster computer system. An example of simultaneously recorded by each camera images is shown in Figures 2(a) and 2(b) together with the corresponding 3D surface elevation field in Figure 2(c).

Four principal uncertainties can be expected in the stereo method: in the calibration parameters (calibration error), in the determination of the corresponding pixels (matching error), in the recovery of 3D coordinates (quantization error), and in the determination of the transformation between the camera reference system and the water reference system with the z-axis vertical and pointing upward (camera orientation error). Following the standard calibration procedure,<sup>51</sup> it was verified that uncertainty in calibration produces errors of the order of fraction of a pixel that can be considered negligible. To determine the orientation and displacement error between the camera reference system and the still water surface, the strategy offered by Benetazzo<sup>40</sup> was adopted. This approach has been proved to be accurate in processing field<sup>41,52</sup> and synthetic<sup>46</sup> data.

Mironov *et al.*<sup>53</sup> observed that stereo wave imaging might be affected by the fact that the water surface reflectance is not

Lambertian. However, Benetazzo<sup>40</sup> showed that for highly textured water surfaces the matching error is small, while Jähne<sup>54</sup> indicates that this error is reduced when the wave slope is much larger than the inclination of the stereo camera's optical axis. To minimize matching and quantization errors, competing requirements on the stereo camera system arrangement have to be met. In order to reduce the range error due to quantization, the baseline-to-distance ratio must be large; however, accurate feature points matching requires that this ratio be small.<sup>54,55</sup> Based on the previous experience on stereo wave imaging at the sea,<sup>40,41,46,56</sup> the correspondence problem is negligible for stereo cameras installed with (almost) parallel optical axes and the baseline-to-distance as small as possible (0.07 m in the present experiment). The photometric consistency between the stereo images is demonstrated in an example of the water surface field shown in Figures 2(a) and 2(b).

The discrete nature of the image formation seems to result in a quantization error that is larger than all other error sources. The coordinates of each pixel can suffer from quantization errors of up to 1/2 pixel, with corresponding disparity error as big as 1 pixel. The estimation of the range along the optical axis and of the coordinates in the normal to optical axis directions thus may be inexact, with the error along the optical axis being the dominant one.<sup>40,55,57</sup> The quantization error may be alleviated by using subpixel (fractional pixel) correspondence.<sup>41,58</sup> An elliptical Gaussian weight function was used to increase the accuracy; following Benetazzo *et al.*,<sup>46</sup> a factor of 5 was adopted as a conservative upper bound for the sub-pixel improvement. The quantization error for the geometry of the present study is obtained through a direct 3D computation of a synthetic wavy surface mapped onto the imaged area over a uniform grid with 0.1 cm spacing. Quantization error was

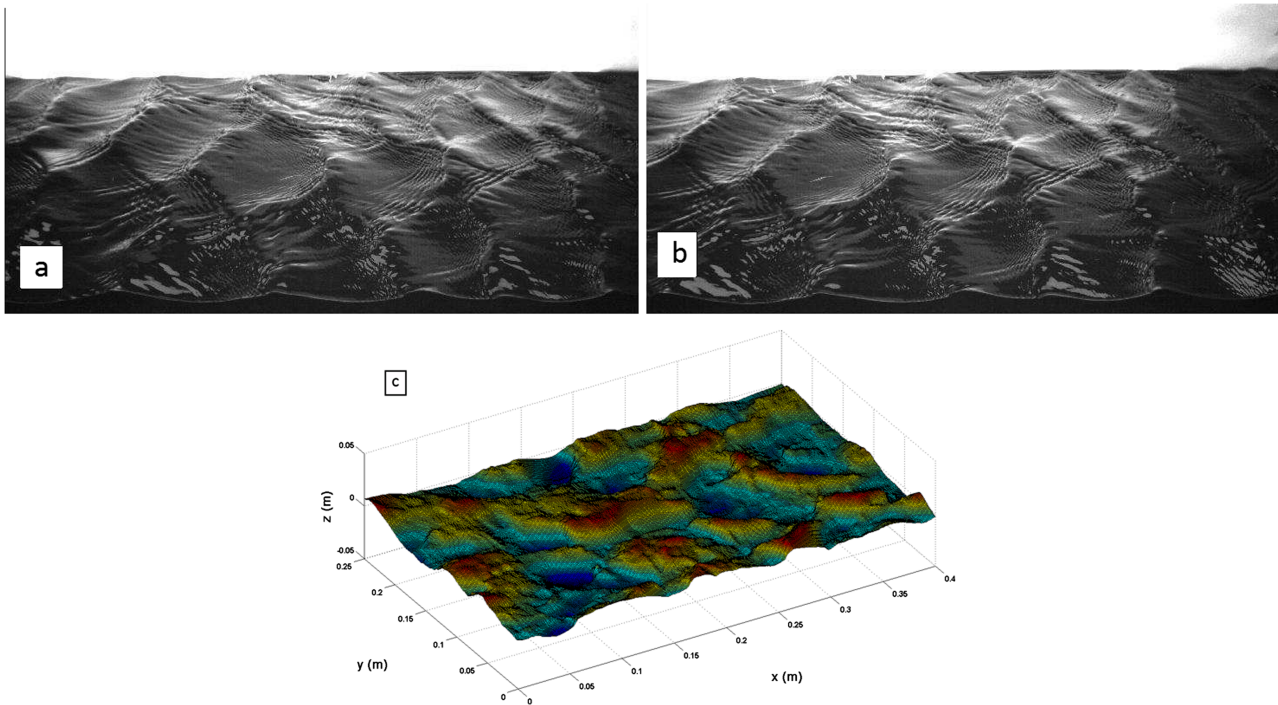


FIG. 2. Stereo imaging: (a) and (b) examples of left and right images captured in the middle of the test section ( $x = 220 \text{ cm}$ ,  $U = 8.5 \text{ m/s}$ ); (c) reconstruction of the water surface from the pair of images.

then computed through a comparison between the original 3D shape and the one retrieved after applying the stereo method. The maximum quantization error along an optical axis of about 0.09 cm was obtained.

### III. QUANTITATIVE COMPARISON OF RESULTS OBTAINED BY DIFFERENT TECHNIQUES

While the capacitance wave gauge is known as a reliable and accurate instrument for measuring the instantaneous surface elevation, the accuracy and the limits of applicability of two other techniques employed in the present study are not yet fully established. It is thus important to verify the results obtained by those methods using wave gauge measurements as a reference.

#### A. Laser slope gauge vs. wave gauge

The laser slope gauge (LSG) so far has been mainly used to image capillary ripples, whereas in the present study the wave field is dominated by much longer gravity-capillary and short gravity waves in the centimeter and decimeter ranges. To verify the capability of LSG to measure accurately the instantaneous 2D surface slope, preliminary tests were conducted on nearly monochromatic waves generated in the flume by a wedge-shaped wave maker. The surface slope was measured by LSG simultaneously with surface elevation measurements by the wave gauge at the same fetch.

The surface elevation and the downwind slope component of the forced harmonic with radian frequency  $\omega_0$  and wavenumber  $k_0$  can be written as

$$\eta(t) = a_0 \cos(k_0 x - \omega_0 t), \quad (1)$$

so that

$$\eta_x(t) = \frac{\partial \eta}{\partial x} = -a_0 k_0 \sin(k_0 x - \omega_0 t). \quad (2)$$

Equations (1) and (2) allow determining  $k_0$  and  $\omega_0$  independently using the linear deep-water dispersion relation

$$\omega_0^2 = k_0 \left( g + \sigma k_0^2 / \rho \right), \quad (3)$$

where  $\rho$  is the water density and  $\sigma$  the surface tension. The time dependence of the surface slope  $\eta_x(t)$  measured by LSG at  $x = 220$  cm is plotted in Figure 3 and compared with that

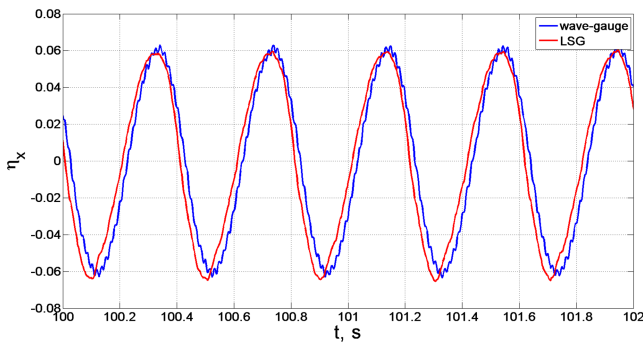


FIG. 3. Comparison of the instantaneous surface slope in the downwind direction measured by LSG and wave-gauge for a mechanically generated wave with period  $T_0 = 0.4$  s and amplitude  $a_0 = 0.25$  cm (wave steepness  $k_0 a_0 = 0.06$ ).

calculated independently from the wave-gauge measurements as

$$\eta_x(t) = \frac{\eta_t(t) \cdot k_0}{\omega_0}. \quad (4)$$

The signal depicting  $\eta_x(t)$  retrieved from the wave-gauge was smoothed using a running average routine. The comparison demonstrates close agreement between the results obtained by the two methods, yielding the same amplitudes and frequencies. The small phase shift between the signals may be attributed to a slight misalignment of the sensors.

Additional experiments were carried out at four forcing frequencies  $f_0 = \omega_0 / 2\pi = 2.5$  Hz, 3 Hz, 3.5 Hz, and 4 Hz that cover the range of dominant frequencies of wind-waves in the experiments. At each prescribed wave frequency  $f_0$ , measurements were performed for several amplitudes; the amplitudes  $a_0$  were selected so that the wave steepness  $k_0 a_0$  did not exceed about 0.13. The maximum wave amplitudes at each frequency were 4.5 mm, 3.5 mm, 2.5 mm, and 2 mm, respectively. For each set of  $a_0$  and  $f_0$ , the wave number  $k_0$  was calculated from the LSG and wave gauge records using (1) and (2). The experimentally derived values of  $k_0$  at each forcing frequency averaged over different amplitudes plotted in Figure 4 agree with the wave numbers corresponding to the linear dispersion relation (3) also plotted in this figure as a dashed curve. The discrepancy between the measured and predicted values varies from 3% at the lowest frequency to 9% for the highest frequency.

Random waves excited in the test section by wind are obviously quite different from the deterministic periodic mechanically generated waves plotted in Figure 3. Records of slope components in the downwind direction,  $\eta_x(t)$  and in the cross-wind direction  $\eta_y(t)$  are compared in Figure 5 with the simultaneously recorded by the wave gauge surface elevation. Both  $\eta_x$  and  $\eta_y$  signals exhibit comparable amplitudes, thus indicating that wind waves are essentially three-dimensional, even though they are excited by a constant, unidirectional and relatively uniform wind in the tank. The slope and the surface elevation records show the frequency of dominant waves about 3 Hz. The shorter capillary waves are not pronounced in the surface elevation record due to their low amplitudes. They are characterized, however, by large surface slopes thus facilitating detection by LSG.

Measurements at identical conditions of surface elevation and slopes enable the determination of wave numbers. Very

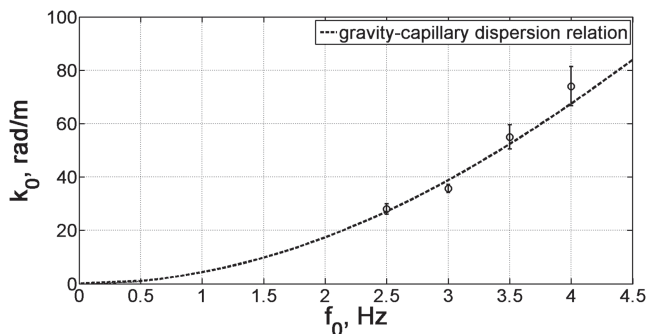


FIG. 4. Experimental results for monochromatic waves (symbols) and the linear dispersion relation (dashed curve).

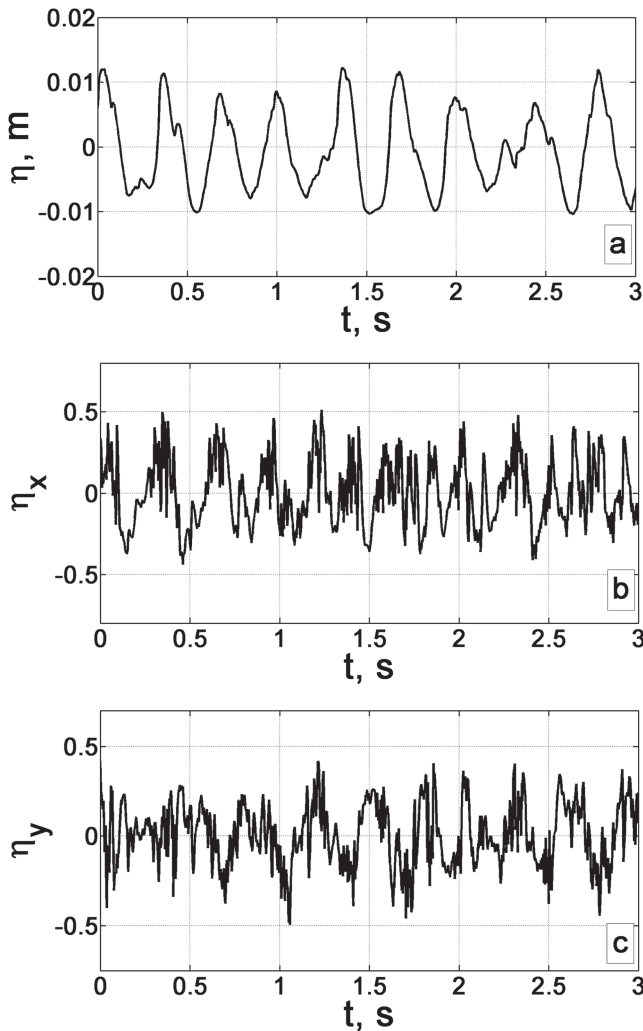


FIG. 5. Synchronized records of (a) surface elevation  $\eta(t)$ , (b)  $\partial\eta/\partial x$ , and (c)  $\partial\eta/\partial y$  at  $x = 340$  cm and  $U = 8.5$  m/s.

short wave may strongly affect the slope records. In analogy with the procedure applied for the deterministic waves, the dominant  $k_x$  wavenumbers based on the LSG measurements of random wind waves were calculated as the ratio between the RMS values of the downwind surface slope, with harmonics exceeding about twice the dominant frequency filtered out, and of the surface elevation measured by the wave gauge. These wavenumbers  $k_x$  were compared in Figure 6 with those calculated using the linear dispersion relation (3) for each dominant frequency.

It can be seen that the measured values of  $k_x$  are consistently lower than the theoretically predicted values. The deviation increases from 9% to almost 30% with the frequency. This difference can be attributed to the Doppler shift caused mostly by Stokes drift and shear flow. The deviation from the linear dispersion relation is more pronounced for shorter waves. Liberzon and Shemer<sup>47</sup> offered an empirical dispersion relation based on simultaneous measurements of wave phase velocity and frequency in the form

$$\frac{k_{gc}}{k} = 1 + a \cdot k + b \cdot k^2, \quad (5)$$

where  $k_{gc}$  is a wavenumber corresponding to the measured dominant frequency according to the relation (3), and  $a$  and  $b$

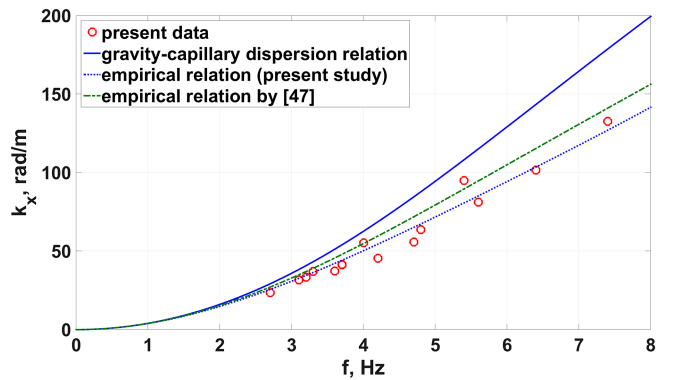


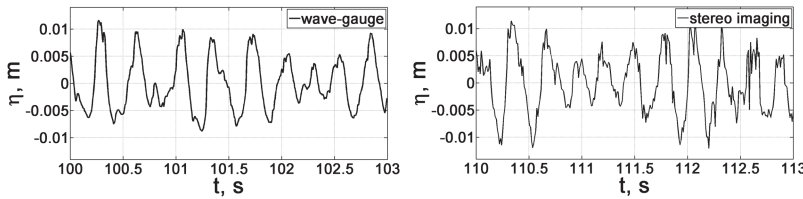
FIG. 6. Variation of the downwind wavenumber  $k_x$  with frequency.

are dimensional empirical coefficients. We adopted this shape of the empirical dispersion relation, the coefficients in (5) estimated from the present data fit are as follows:  $a = 0.006$  m;  $b = -2.2 \times 10^{-5}$  m<sup>2</sup>. The curve that corresponds to the dispersion relation of Liberzon and Shemer<sup>47</sup> was obtained for a narrower range of frequencies is also plotted in Figure 6 for comparison. The two curves do not differ significantly (within 3%–9% for the frequency range  $2.4$  Hz  $< f < 7.5$  Hz). This agreement between the dependence of wavenumbers of short wind waves on frequency in the presence of induced current obtained by two unrelated methods serves as an additional evidence of the accuracy of the ability of LSG to provide quantitative information on the wind wave field in the range of dominant frequencies pertinent to this study.

## B. Video stereo imaging

Surface elevation variation with time at a fixed location  $\eta(x; t)$  can be retrieved from the reconstructed 3D surfaces derived from the stereo imaging. These records can be compared with the wave-gauge results at an identical wind velocity and fetch. Note, however, that stereo video and wave gauge records cannot be acquired simultaneously at the same fetch. Short segments of time series recorded by the two methods are plotted in Figure 7 for the fetch  $x = 340$  cm and wind velocity  $U = 8.5$  m/s. For these conditions only, the processing of a stereo record taken at the full rate of 100 fps within vicinity of a single point in the center of the imaged area was performed. The two signals have comparable wave heights and dominant frequencies, although the stereo imaging yields a noisier record. The dominant period of the wave in both records is about 0.3 s.

To enable quantitative comparison, root mean square (RMS) values of the surface elevation,  $(\overline{\eta^2})^{1/2}$ , were calculated from the data obtained by these techniques at all wind velocities and fetches; see Figure 8. The RMS values from the reconstructed surfaces are computed by averaging the RMS of time series taken from the virtual wave-gauges located across the central part of the images. Prior to computing the RMS values, the time series obtained by both methods were band-pass filtered in the frequency range of 1–10 Hz. The results are spread relatively close to the  $45^\circ$  line. Taking the wave gauge results as a reference, the stereo imaging method overestimates the  $(\overline{\eta^2})^{1/2}$  values for small-amplitude waves by up to 30% for the lowest wind velocity and underestimates the



values of the surface elevation fluctuations exceeding 5 mm by less than 15% for the highest wind velocity.

Next, the frequency spectra of the surface elevation variation in time obtained by the stereo imaging and by the wave-gauge are compared in Figure 9. In view of inaccuracy of stereo imaging of low amplitude waves, see Figure 8, the spectra were computed for all experimental conditions, but the comparison carried out only for the moderate and high wind forcing at the middle and longest fetches. To calculate frequency spectra, the accumulated wave gauge records were divided into windows with a duration of 25.6 s, with 50% overlap, thus yielding over 900 independent spectral estimates. Averaging of the power spectra over all windows was then performed.

To enlarge the ensemble for the computation of frequency spectra based on the reconstructed 3D surfaces, the time series from 50 virtual probes, located at different locations in the crosswind direction within the central part of the imaged area were retrieved. To enable quantitative comparison with the wave gauge data, the spectra based on the 3D reconstruction were also computed for a window duration of 25.6 s. The resulting power spectra over the whole ensemble of data that contained more about 250 independent spectral estimates were obtained by averaging. It can be seen that, although not identical, the spectra obtained by different techniques exhibit similarity in all examined cases. The spectra within about 30% of the peak frequency are quite close for all cases, whereas away from the dominant frequency, and thus for notably smaller wave amplitudes, the deviations increase.

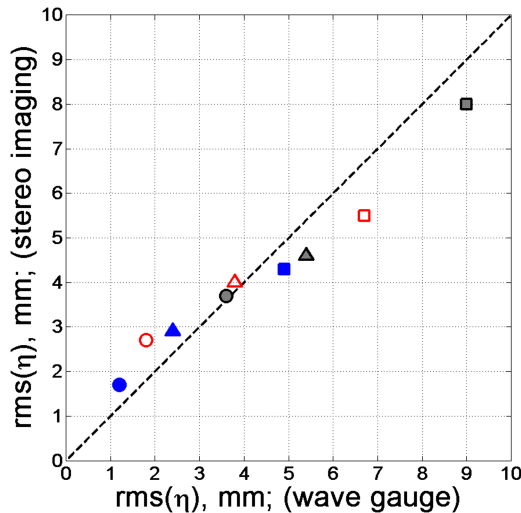


FIG. 8. Comparison of  $(\overline{\eta^2})^{1/2}$  obtained by stereo video imaging (vertical axis) and by a wave gauge (horizontal axis). Each point represents the result obtained by both methods at identical conditions. Symbols denote the wind velocity: circles— $U = 6.5$  m/s, triangles— $U = 8.5$  m/s, squares— $U = 10.5$  m/s; color (style) denotes the fetch: blue (filled)— $x = 120$  m; red (open)— $x = 220$  m; black edge gray face— $x = 340$  m.

FIG. 7. Variation of the surface elevation with time at  $x = 340$  cm and  $U = 8.5$  m/s acquired by two methods: by a wave-gauge (left panel) and by stereo imaging (right panel). Records are not synchronized, the time reference is arbitrary.

The disparity between the spectral values in Figure 9 is consistent with the corresponding difference in the RMS values of the surface elevation as seen in Figure 8. The origins of inaccuracy in results derived from the virtual probes in the 3D reconstruction may be traced to the processing procedure applied. The mesh of desirable resolution is established within the common to the two cameras' rectangular area of the water surface and is then held fixed for the whole series of the images acquired at the given wind-fetch conditions. However, a slight deviation of the mean value of the water surface with time may lead to a shift in the boundaries of the reconstructed surfaces in the crosswind direction, thus causing jitter in the location of the virtual probe. This spatial jitter can cause error in the time series of the surface elevation retrieved from the stereo image reconstruction. The non-negligible quantization error can also contribute to less than desirable accuracy of the stereo reconstruction.

It thus transpires that at the currently available resolution, stereo imaging is capable of providing information on the gross features of the wave field, while yielding detailed information that may be inaccurate. This is in general agreement with Jähne *et al.*<sup>57</sup> who maintained that stereo imaging is restricted to measuring large-scale structures only. Due to technical constraints mainly related to the limited computer power, this observation seems to remain relevant two decades later, although fast improvements in the processing algorithms

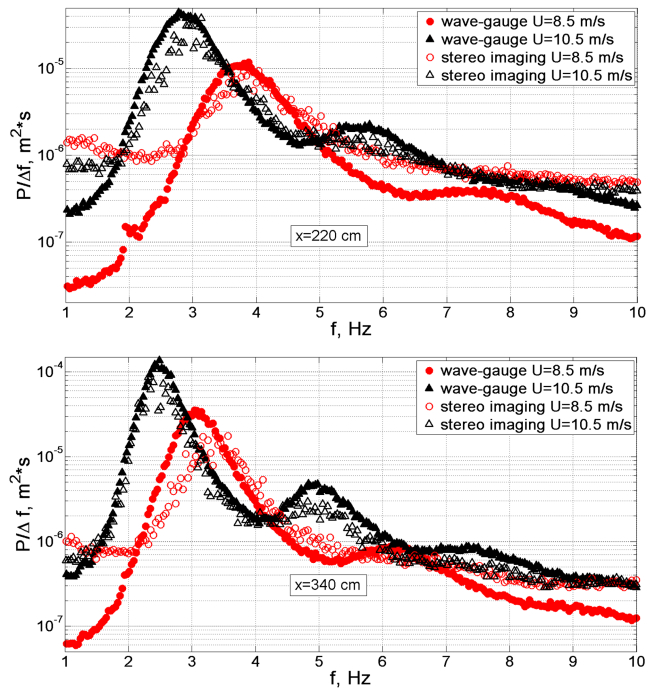


FIG. 9. Comparison of power spectra of the surface elevation measured by a wave-gauge and stereo imaging.

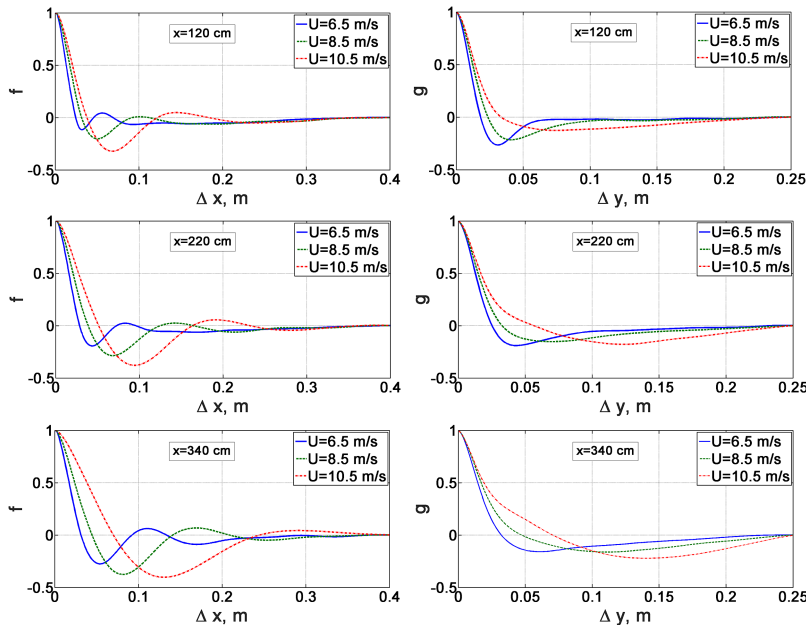
may eventually make this restriction obsolete. It should also be mentioned that the space limitations around the experimental facility posed significant restrictions on the possible arrangement of the cameras, thus reducing the ability to minimize the quantization error by adjusting the camera inclination angle and the base distance.

#### IV. SPATIAL STRUCTURE OF THE WIND-WAVE FIELD

The major advantage offered by the stereo imaging over the alternative measuring methods is thus in its ability to characterize the global structure of the wind-wave field. This can be done using the spatial autocovariance functions. The autocovariance function

$$f(\Delta x) = \frac{\eta(x)\eta(x + \Delta x)}{\eta(x)^2} \quad (6)$$

in the downwind direction was calculated along the imaged area for 3 constant values of the spanwise coordinate  $y$ ; the reference value of  $x$  was taken at the right (upwind) end of the image. The resulting functions  $f(\Delta x)$  were averaged over various values of  $y$  and then over all reconstructed surfaces. Results for different fetches and wind velocities  $U$  are plotted in Figure 10. In all cases, the autocovariance functions decay relatively fast and effectively attain zero after the second local minimum. In analogy with a deterministic monochromatic wave, where the autocovariance function is given by a cosine, the value of  $\Delta x$  at the first local minimum in Figure 10 corresponds to a half of the local dominant wavelength  $\lambda_d$ . In view of spatial inhomogeneity of the wave field, the values of autocovariance function  $f(\Delta x)$  were computed by direct integration without invoking the Fourier transform that implies periodicity. Note that due to increasing with the fetch wavelength, the first maxima in the left column of Fig. 10 are located at distances that somewhat exceed  $\lambda_d$ . The estimated wavelengths range from 7 cm to 27 cm that according to the dispersion relation (5) correspond to dominant frequencies ranging from 2.4 Hz to 4.7 Hz.



The averaged autocovariance functions in the crosswind direction,

$$g(\Delta y) = \overline{\frac{\eta(y)\eta(y + \Delta y)}{\eta(y)^2}}, \quad (7)$$

are plotted in the right column of Figure 10. In this case, the averaging was first performed over 3 different constant values of  $x$  within the reconstructed surface elevation map; subsequent averaging was carried out over the whole set of the instantaneous reconstructed surfaces.

It is somewhat surprising that the minima and maxima of the autocovariance functions  $g(\Delta y)$  shown in the right column of Figure 10 which represent the wave field structure in the crosswind direction are located at displacements that do not differ notably from those in the left column of Figure 10. This observation thus confirms that the wind-waves at those fetches are short-crested and three-dimensional.

For the shorter fetch and lower wind velocity, the absolute value of the minimum  $g(\Delta y)$  is larger than that of  $f(\Delta x)$ . Values and distances of the 1st minima of  $f(\Delta x)$  and  $g(\Delta y)$  and of the 2nd maxima of  $f(\Delta x)$  are summarized in Tables I and II, respectively. Both functions  $f(\Delta x)$  and  $g(\Delta y)$  effectively vanish at distances that do not exceed significantly the dominant wave length, indicating that surface elevation records at those distances are statistically independent.

The value of the 1st minimum of the autocovariance function  $f(\Delta x)$  provides a qualitative estimate of the spectral width.<sup>39</sup> For a deterministic monochromatic wave, the absolute value of the minimum is unity. As the spectrum widens, the absolute minimum value of  $f(\Delta x)$  decreases, ranging in the left column of Figure 8 from 0.1 to 0.45. Note that for a given fetch, the absolute minimum values increase with wind velocity  $U$  thus indicating that the spectrum becomes narrower, in agreement with findings of Zavadsky *et al.*<sup>1</sup> The absolute minimum values of  $g(\Delta y)$  in the right column of Figure 8 are notably lower than for  $f(\Delta x)$ , with an exception of the very short fetch,  $x = 120$  cm.

FIG. 10. Spatial autocorrelation functions  $f(\Delta x)$  (left column) and  $g(\Delta y)$  (right column) at various fetches.

TABLE I. Values of the 1st minima of  $f(\Delta x)$  and  $g(\Delta y)$  and of the 2nd maxima of  $f(\Delta x)$ .

Fetch, cm U, m/s	120			220			340		
	Min $f(\Delta x)$	Max $f(\Delta x)$	Min $g(\Delta y)$	Min $f(\Delta x)$	Max $f(\Delta x)$	Min $g(\Delta y)$	Min $f(\Delta x)$	Max $f(\Delta x)$	Min $g(\Delta y)$
6.5	0.15	0.03	0.29	0.22	0.01	0.23	0.33	0.052	0.14
8.5	0.22	0.02	0.19	0.28	0.03	0.18	0.36	0.049	0.17
10.5	0.28	0.06	0.17	0.38	0.07	0.17	0.4	0.043	0.22

Integral length scales characterize the extent of coherence of the wind-wave field. The scales in the downwind,  $\Lambda_x$ , and crosswind,  $\Lambda_y$ , directions can be defined as follows:

$$\Lambda_x = \int |f(x)|dx, \quad (8)$$

$$\Lambda_y = \int |g(y)|dy. \quad (9)$$

Similarly to the dominant wavelengths, both length scales  $\Lambda_x$  and  $\Lambda_y$  increase with the wind velocity and with the fetch. These integral scales are plotted in Figure 11 after being normalized by the local characteristic scale of wind waves,  $\lambda_d$ . The dominant wind-wave lengths  $\lambda_d$  were determined for each fetch and wind velocity from the dominant frequency  $f_d$  using the empirical dispersion relation (5). The results of Figure 11 demonstrate that the integral scales  $\Lambda_x$  and  $\Lambda_y$  are notably smaller than the dominant wavelengths  $\lambda_d$ , with  $\Lambda_x/\lambda_d$  ranging from 1.2 to 2. These results are qualitatively different from those reported by Paquier *et al.*<sup>34</sup> in their experiments with short gravity-capillary wind-waves in a viscous fluid.

Both  $\Lambda_x/\lambda_d$  and  $\Lambda_y/\lambda_d$  decrease with the fetch and with the wind velocity; the effect of the wind velocity of the normalized integral scales appears to decrease with the fetch. The values of  $\Lambda_x/\lambda_d$  and  $\Lambda_y/\lambda_d$  indicate that although the wind-waves propagate in a relatively narrow channel with the mean wind velocity directed along the test section, the waves are in fact extremely short crested, and cease to be coherent at distances much shorter than the dominant wavelength. In view of results presented in the right panel of Figure 11 and the range of  $\lambda_d$  in this study, the data taken along the lines  $y = \text{const.}$  that are separated by more than about 5 cm can be considered as statistically independent.

Neglecting the spatial inhomogeneity of the wave field within the imaged area, directional spectra  $S(k, \theta)$  were calculated from the reconstructed surfaces. Here  $k = (k_x^2 + k_y^2)^{1/2}$  is the wavenumber and  $\theta = \tan^{-1}(k_y/k_x)$ . The resulting power spectra were then averaged over the whole set of reconstructed surfaces. The spectra at all fetches and for all wind velocities are presented in Figure 12. Directional ambiguity can be

resolved in most cases since the direction of wind is from the right to the left.

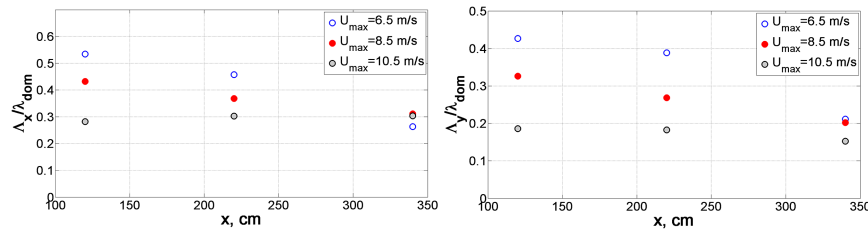
The spectra at low wind velocities and shorter fetches are characterized by the presence of waves in the crosswind direction. The question of directional ambiguity thus remains open for those cases, although symmetry considerations suggest that waves propagating in both positive and negative  $y$  directions are present. The direction of the dominant wave for moderate winds deviates slightly to the left of the wind direction; this may suggest that the reconstruction procedure for low elevations introduces directional inaccuracy.

It should be noted, however, that Cailliez and Collard<sup>60</sup> who performed the reconstruction of the decimeter-scale water wave surface based on simultaneous imaging of the wave slopes in two perpendicular directions, also report on asymmetry in the directional spectra at early stages of wind-waves evolution. At high wind speeds and larger fetches, as the dominant waves become longer and higher, this asymmetry disappears; the peaks of the directional spectra are at  $180^\circ$ . The azimuthal angle of  $0^\circ$  corresponds to the windward slope and  $180^\circ$  to the leeward direction. The wave numbers associated with the dominant waves in those cases agree within at most 15% with the results obtained from the autocorrelation function. The only exception represents the case of the highest wind speed and the longest fetch, where the value of the wavelength is overestimated in the spectral representation due to an insufficient image size that is comparable with the wavelength. The directional spreading of the spectrum in most cases is up to  $60^\circ$  around the wind direction. This finding corroborates the conclusion reached from the analysis of autocorrelation functions that wind-waves are essentially three-dimensional and short crested even in a relatively narrow channel.

Another approach to study the three-dimensionality of wind waves was based on the LSG. Comparison of the RMS values of both the downwind  $\eta_x(t)$  and crosswind  $\eta_y(t)$  slope components is carried out in Figure 13 together with the RMS of the total slope  $\sqrt{\eta_x^2 + \eta_y^2}$ .

TABLE II. Locations of the 1st minima of  $f(\Delta x)$  and  $g(\Delta y)$  and of the 2nd maxima of  $f(\Delta x)$ .

Fetch, cm U, m/s	120			220			340		
	Min $f(\Delta x)$	Max $f(\Delta x)$	Min $g(\Delta y)$	Min $f(\Delta x)$	Max $f(\Delta x)$	Min $g(\Delta y)$	Min $f(\Delta x)$	Max $f(\Delta x)$	Min $g(\Delta y)$
6.5	0.03	0.06	0.03	0.05	0.09	0.04	0.06	0.11	0.06
8.5	0.05	0.11	0.04	0.07	0.15	0.07	0.08	0.17	0.10
10.5	0.07	0.15	0.08	0.1	0.2	0.11	0.13	0.3	0.12



The RMS values of both surface slope components are of the same order, with the downwind components  $\eta_x$  exceeding those of  $\eta_y$  for each wind velocity  $U$ . These findings provide additional evidence for the three-dimensional structure of wind waves studied in the present experiments and are consistent with the spatial autocorrelation results presented in Figures 10 and 11. At constant  $U$ , the values of both slopes exhibit certain scatter without any detectable trend. Both characteristic surface slope components and the total slope increase somewhat with the wind velocity. The ratio of the RMS values of both slope components seems to decrease with the wind velocity.

Additional insight into the characteristic wind-wave geometry can be gained from analyzing the directions of the instantaneous surface slope represented by the projection of normal to the surface on the horizontal plane. The probability density functions (PDFs) of azimuthal angles of the instantaneous surface inclination are presented in Figure 14(a) for the representative wind velocity  $U = 8.5$  m/s and three fetches, and in Figure 14(b) for the fetch  $x = 220$  cm and various wind velocities. For each fetch and wind velocity, the results are based on the ensemble of  $2.4 \times 10^6$  measurements of both components of the instantaneous slope. The probability distributions of the slope inclination direction in Figure 14(a) do

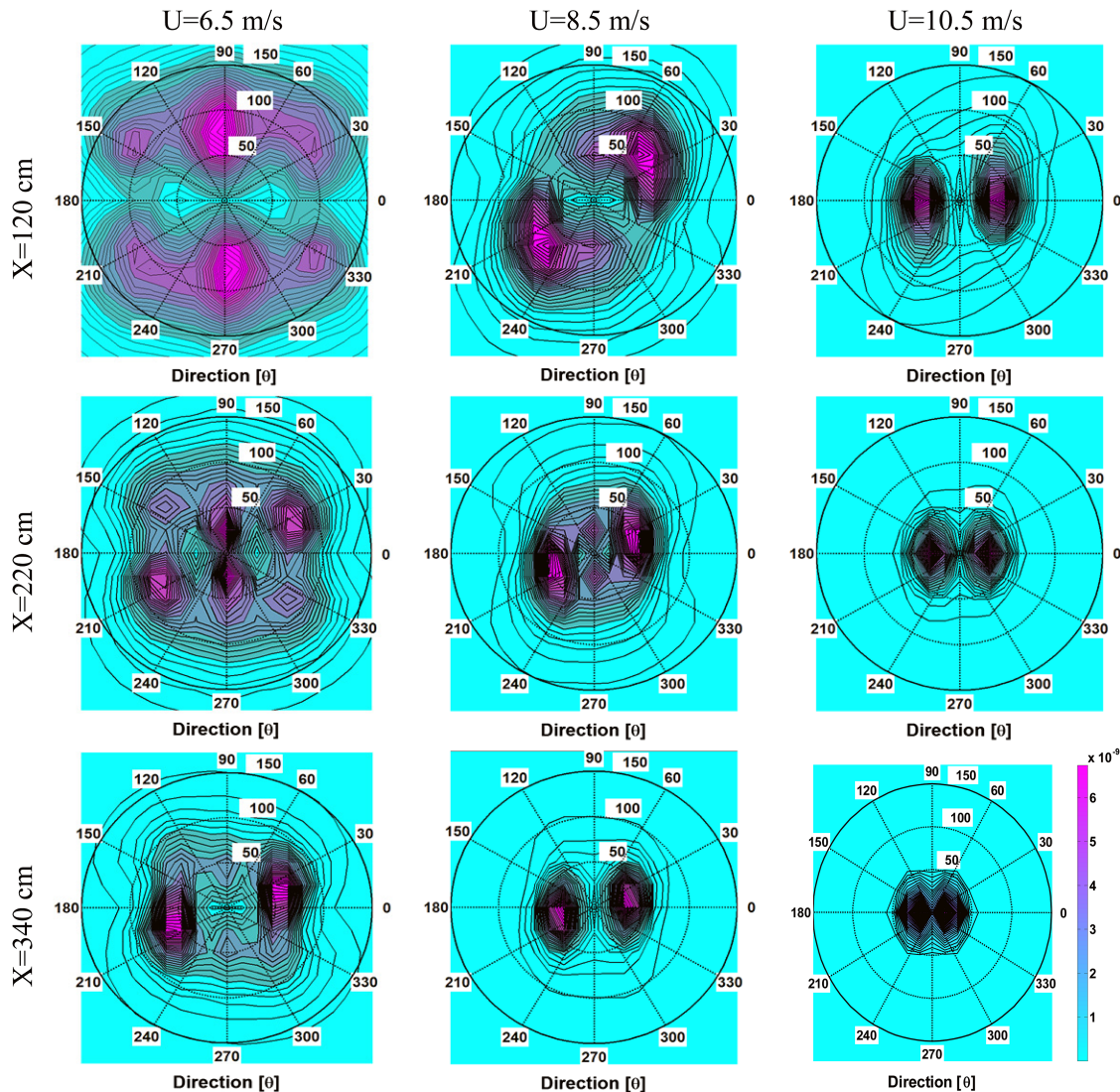


FIG. 12. The directional spectra, wind direction from right to left (scale bar [ $m^{-4}$ ]).

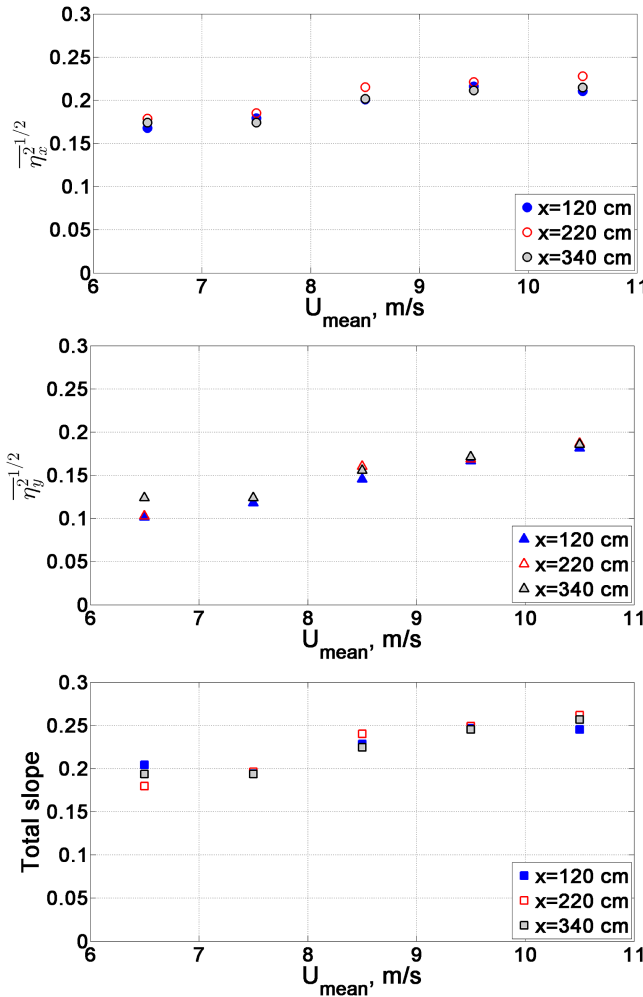


FIG. 13. Variation of the RMS values of the surface slope components and of the total slope with the wind velocity for various fetches.

not vary notably with the fetch; similar behavior was obtained for all other wind velocities. The effect of the wind velocity on the PDF of the slope direction is much more noticeable, Figure 14(b). Unlike the results presented in Figure 12, the probability distribution functions in Figure 14, as well as in all other cases not shown in this figure, exhibit symmetry around the channel axis. However, the directional spreading is very similar for both spectral and PDF representations.

All curves in Figure 14 are characterized by two distinctive peaks at  $0^\circ$  and  $180^\circ$ , which indicate that the prevailing direction of the waves is aligned with that of wind. Nevertheless, the probability of the instantaneous surface inclination in all other directions, including crosswind, is not negligible.

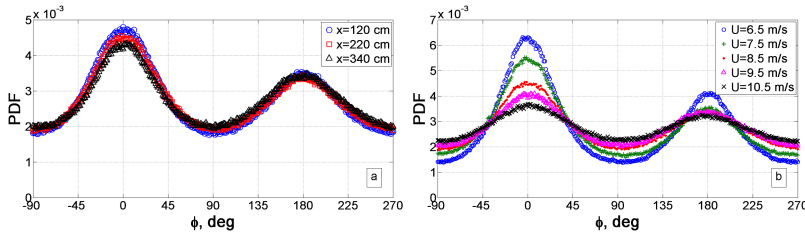


FIG. 14. Probability density function of the slope inclination direction: (a) for  $U = 8.5$  m/s and different fetches; (b) for the fetch  $x = 220$  cm and different wind velocities.

The probability of the leeward slope is notably lower than that of the windward inclination. This asymmetry in the peak values in Figure 14 can be attributed to the pronounced asymmetry of the shape of steep wind waves, with a leeward part on the average shorter than the windward part, as seen in a snapshot of the typical wind-wave profile presented in Figure 15. Figure 14(b) clearly demonstrates that with increasing wind velocity, resulting in longer dominant waves, the PDF becomes flatter and the maxima in the  $x$  direction become less pronounced, and the probability of the instantaneous slope in the crosswind direction increases.

Short parasitic ripples on the leeward part of the wave are clearly visible in Figure 15. The presence of these ripples is characteristic for the decimeter-range wind waves.<sup>11</sup> The parasitic ripples, however, apparently do not affect notably the probabilities of slope inclinations.

The temporal autocovariance function defined in analogy with (6) and (7) as

$$h(\Delta t) = \frac{\overline{\eta(t)\eta(t + \Delta t)}}{\overline{\eta(t)^2}} \quad (10)$$

is plotted in Figure 16(a) for the surface elevation derived from wave gauge measurements for the wind velocity  $U = 10.5$  m/s at all three fetches. The absolute value of  $h(\Delta t)$  at the 1st minimum is about 0.65–0.78, much larger than the corresponding values in Figure 10. This difference may be attributed to two factors. First, the wavenumber spectrum is wider than the frequency spectrum (approximately by a factor of 2 for pure gravity waves). In addition, the fetch-limited wave field in the current experiments is statistically stationary but spatially inhomogeneous. The spatial variation of the wind-wave field over the expanse of the image causes an additional widening of the spectral band.

It is instructive to compare the temporal autocovariance function retrieved from the virtual wave gauge at a single point of the reconstructed surfaces from stereo imaging and the corresponding autocovariance function calculated from the measurements carried out by a real wave gauge. The two functions computed for similar conditions are plotted in Figure 16(b). The locations of the first local minima differ by 0.012 s; the difference between subsequent corresponding local minima and maxima grows as an integer multiple of this value. This deviation may be attributed to a slight shift in the actual measuring locations by the two methods. The absolute values of the maxima and minima of the autocovariance function obtained from the wave gauge data exceed the corresponding values based on the stereo video imaging, apparently as a result of higher accuracy of the wave gauge measurements and a relatively coarse grid adopted in the stereo

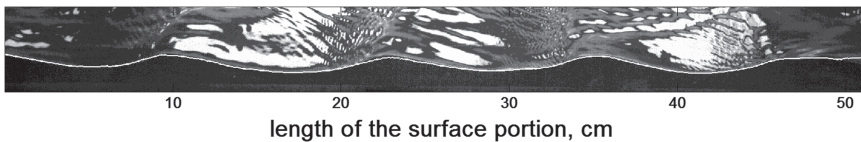


FIG. 15. Snapshot of the wave profile as it is seen through the transparent wall of the flume with the contact line enhanced, wind direction from right to left (fetch  $x = 220$  cm,  $U = 8.5$  m/s).

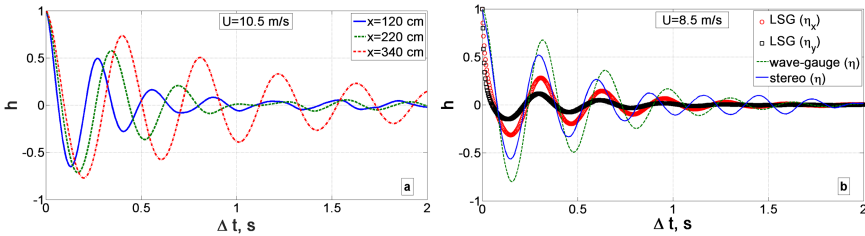


FIG. 16. Temporal autocorrelation function  $h(\Delta t)$  at  $x = 340$  cm: (a) wave gauge measurements at three wind velocities; (b) comparison of results derived from different techniques.

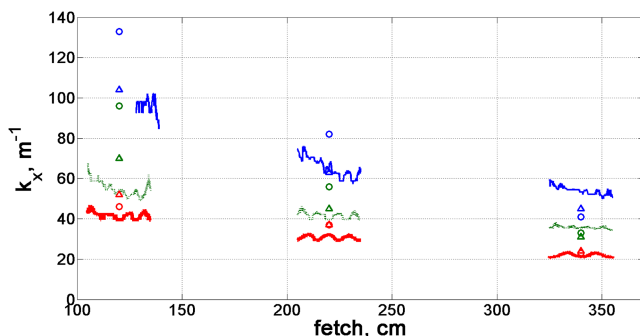


FIG. 17. Variation of the wavenumber values along the test section: line—wavelet transform of 3D surfaces, circle—RMS from LSG measurements, triangle—autocorrelation of 3D surfaces; blue— $U = 6.5$  m/s, green— $U = 8.5$  m/s, red— $U = 10.5$  m/s.

reconstruction procedure. The temporal autocovariance functions for the slope component variations that are also plotted in Figure 16(b) have lower maxima and minima values and decay faster. The location of the first local minimum of the surface slopes differs by about 0.005 s from the one of the surface elevation.

The values of the dominant wavenumber at each wind velocity and fetch condition can be compared using the independently collected data from the stereo imaging and from the LSG. Since the wave field is spatially inhomogeneous, wavelet transform was applied to process stereo-derived images; this approach proved to be advantageous to the application of short spatial extent Fourier transform due to its limited resolution. The real Morlet wavelet (see, e.g., Fuga<sup>[6]</sup>) conventionally used for a nonstationary temporally varying process was chosen and adapted to the spatial form.

The wavelet-derived wavenumbers are compared in Figure 17 at each wind-fetch condition with the local values of  $k_x$  derived from the LSG measurements. In addition, wavenumbers based on the location of the 1st minimum of the autocorrelation function  $f(\Delta x)$  given in Table II are also presented. There is a continuous growth of the wavelength (or decay of the wavenumber) along the tank depicted by all techniques applied in the present study; the wavelet analysis demonstrates that the spatial inhomogeneity of the wave field may be detected even along the relatively short imaged frame.

There is a reasonable agreement between the wavenumbers obtained by different methods; in some cases, the agreement is nearly perfect. In general, very good agreement (within few per cent) was obtained for higher wind velocities at the longer fetch  $x = 330$  cm, the difference in  $k_x$  values obtained at this fetch by the two methods increases at lower wind velocities up to roughly 10% and becomes even larger at shorter fetches attaining about 30% at  $x = 120$  cm,  $U = 6.5$  m/s. As could be expected, for short waves of low amplitude, results obtained by various techniques exhibit a notable scatter.

## V. DISCUSSION AND CONCLUSIONS

The behavior of short gravity waves in a wind wave tank was investigated using optical measuring techniques along with the conventional wave gauge. A stereo video imaging system and a laser slope gauge (LSG) were used extensively in a small experimental facility. In this study, the stereo imaging technique was utilized in a laboratory facility at multiple experimental conditions for the first time. An extensive set of data accumulated by applying independent measuring techniques allows examining the accuracy and the limits of application of each method. The results enable drawing some conclusions regarding the spatial structure and variability of young waves excited by wind in controlled laboratory conditions.

The efficiency of fast stereo video imaging to study wind-waves in a laboratory facility is clearly demonstrated. It should be stressed, though, that the application of this technique is far from being straightforward. While in the field studies, a uniform illumination of sufficient intensity is often available under normal operational conditions; our experience indicates that considerable effort has to be invested to attain an appropriate illumination in a closed laboratory. Space limitations can also affect the spatial coverage of the recorded images. The available algorithms to retrieve the spatial distribution of the surface elevation from pairs of video images also impose severe restrictions on the spatial and temporal resolutions of the measurements, as well as on their duration, even when parallel processing using multiple cores is applied. Recent advances on the stereo processing of sea surface waves<sup>[56]</sup> highly reduced the computational resources required to

analyze a sequence of stereo images. It thus can be expected that the computer limitations constitute only a temporary impediment to wider application of this method. The developments in the image processing algorithms and increased computer power will certainly lead to the improvement of the spatial and temporal resolutions of the reconstructed images and to wider spreading of this technique. It can be predicted with confidence that in not too distant future stereo video imaging will become a standard tool for the investigation of waves in laboratory.

Despite the limitations of the method, the time-resolved stereo video imaging of the wind-wave field applied in the present study proved to be a powerful instrument in studying wind waves, providing novel qualitative and to certain extent quantitative information on waves. The RMS values of the surface elevation variation retrieved from the stereo images and those measured by a wave gauge at identical forcing conditions demonstrate that processing of stereo images is capable of presenting the global features of the wave field. The ability of the stereo imaging technique to follow more subtle wave characteristics such as the temporal variation of the surface elevation has also been examined by inspecting the spectra of the surface elevation calculated from the virtual probes within the reconstructed images. In the main peak region for different fetches and wind velocities, the frequency spectra derived from stereo video imaging demonstrate qualitative agreement with the spectra obtained from the conventional wave gauge records. Away from the dominant frequency, the agreement between the spectra deteriorates, indicating that the sensitivity of stereo imaging in its present implementation to small surface elevation variations is limited.

These observations give some confidence to the validity of stereo video results in general and in particular in the qualitative features characterizing the directional wave vector spectra; note that this information often cannot be directly acquired by other methods. Certain left-right asymmetry in the directional spectra at shorter fetches may be attributed to some systematic error of the reconstruction process. However, a qualitatively similar asymmetry of spectra that has been reported for comparable operational conditions by Caulliez and Collard<sup>60</sup> suggests that very young wind-waves indeed propagate in directions that are different from that of the wind, and in fact may be normal to the wind direction at the initial stages of evolution.

Availability of multiple “snapshots” of the instantaneous surface elevation under a variety of conditions enables the computation of the spatial autocorrelation functions in along- and crosswind directions that were used to define integral length scales in the two directions. These scales provide a measure of distances at which the waves retain their coherence and are considerably shorter than the corresponding dominant wavelengths. The major result of this study is that the instantaneous wind-wave field is thus essentially random and three-dimensional at all operational conditions. This observation based on stereo video imagery is consistent with findings resulting from LSG measurements that show slopes in the  $x$  and  $y$  directions of comparable value, as well as wide spreading of the instantaneous surface inclination angles evident in the results plotted in Figure 14.

The strong three-dimensionality of the random wind-wave field and virtual absence of correlation attained already at short distances indicate that the evolving wave field is effectively insensitive to the existence of sidewalls in the tank. It is well known that coherent spatial disturbances in a narrow channel cause excitation of cross-, or sloshing, waves with lateral wavenumbers commensurate with the channel’s width that due to their resonant character grow fast and dominate the wave field (Shemer<sup>62</sup> and the references therein). No such waves were observed in the present experiments after the shutdown of the blower. The lack of spatial coherence thus enables meaningful experiments on 3D wind-waves in a quite narrow wind tank.

The LSG is another nonintrusive optical technique that has been used extensively in this study. The extensive measurements performed with LSG made it possible to substantiate statistically the asymmetry between the windward and leeward sides of the waves, which was often reported based on limited one-dimensional observations. The RMS values of the slope components  $\eta_x$  and  $\eta_y$  provide additional evidence of three-dimensionality of the wind wave field.

## ACKNOWLEDGMENTS

This research was supported by the Israel Science Foundation (Grant No. 306/15), by the Italian Ministry of Foreign Affairs, and partially by the Flagship Project RITMARE—The Italian Research for the Sea-coordinated by the Italian National Research Council and funded by the Italian Ministry of Education, University and Research within the National Research Program 2011–2015.

- <sup>1</sup>A. Zavadsky, D. Liberzon, and L. Shemer, “Statistical analysis of the spatial evolution of the stationary wind wave field,” *J. Phys. Oceanogr.* **43**, 65 (2013).
- <sup>2</sup>H. Mitsuyasu, “On the growth of the spectrum of wind-generated waves. I,” *Rep. Res. Inst. Appl. Mech. (Kyushu Univ.)* **16**, 459 (1968).
- <sup>3</sup>H. Mitsuyasu and T. Honda, “The high frequency spectrum of wind-generated waves,” *J. Oceanogr. Soc. Japan* **30**, 185 (1974).
- <sup>4</sup>D. E. Hasselmann, M. Dunckel, and J. A. Ewing, “Directional wave spectra observed during JONSWAP 1973,” *J. Phys. Oceanogr.* **10**, 1264 (1980).
- <sup>5</sup>K. K. Kahma, “A study of the growth of the wave spectrum with fetch,” *J. Phys. Oceanogr.* **11**, 1503 (1981).
- <sup>6</sup>K. K. Kahma and C. J. Calkoen, “Reconciling discrepancies in the observed growth of wind-generated waves,” *J. Phys. Oceanogr.* **22**, 1389 (1992).
- <sup>7</sup>W. J. Plant, “A relationship between wind stress and wave slope,” *J. Geophys. Res.* **87**, 1961, doi:10.1029/JC087iC03p01961 (1982).
- <sup>8</sup>H. Mitsuyasu, Y. Y. Kuo, and A. Masuda, “On the dispersion relation of random gravity waves. Part 2. An experiment,” *J. Fluid Mech.* **92**, 731 (1979).
- <sup>9</sup>D. W. Wang and P. A. Hwang, “The dispersion relation of short wind waves from space-time wave measurements,” *J. Atmos. Oceanic Technol.* **21**, 1936 (2004).
- <sup>10</sup>M. Donelan, A. Babanin, E. Sanina, and D. Chalikov, “A comparison of methods for estimating directional spectra of surface waves,” *J. Geophys. Res.* **120**, C010808, doi:10.1002/2015JC010808 (2015).
- <sup>11</sup>M. Perlin, H. Lin, and C.-L. Ting, “On parasitic capillary waves generated by steep gravity waves: An experimental investigation with spatial and temporal measurements,” *J. Fluid Mech.* **255**, 597 (1993).
- <sup>12</sup>X. Liu and J. H. Duncan, “The effects of surfactants on spilling breaking waves,” *Nature* **421**, 520 (2003).
- <sup>13</sup>G. V. Strum and F. Y. Sorrell, “Optical wave measurement technique and experimental comparison with conventional wave height probes,” *Appl. Opt.* **12**, 1928 (1973).
- <sup>14</sup>G. Tober, R. C. Anderson, and O. H. Shemdin, “Laser instrument for detecting water ripple slopes,” *Appl. Opt.* **12**, 788 (1973).

- <sup>15</sup>B. A. Hughes, H. L. Grant, and R. W. Chappel, "A fast response surface-wave slope meter and measured wind-wave moments," *Deep Sea Res.* **24**, 1211 (1977).
- <sup>16</sup>C. S. Palm, R. C. Anderson, and A. M. Reece, "Laser probe for measuring 2-D wave slope spectra of ocean capillary waves," *Appl. Opt.* **16**, 1074 (1977).
- <sup>17</sup>A. M. Reece, "Modulation of short waves by long waves," *Boundary Layer Meteorol.* **13**, 203 (1978).
- <sup>18</sup>S. J. Miller, O. H. Shemdin, and M. S. Longuet-Higgins, "Laboratory measurements of modulation of short-wave slopes by long surface waves," *J. Fluid Mech.* **233**, 389 (1991).
- <sup>19</sup>A. V. Fedorov, W. K. Melville, and A. Rozenberg, "An experimental and numerical study of parasitic capillary waves," *Phys. Fluids* **10**, 1315 (1998).
- <sup>20</sup>G. Cailliez and C.-A. Guérin, "Higher-order statistical analysis of short wind wave fields," *J. Geophys. Res.* **117**, C06002, doi:10.1029/2011JC007854 (2012).
- <sup>21</sup>J. D. Barter, K. L. Beach, and P. H. Y. Lee, "Collocated and simultaneous measurement of surface slope and amplitude of water waves," *Rev. Sci. Instrum.* **64**, 2661 (1993).
- <sup>22</sup>M. A. Donelan and W. J. Plant, "A threshold for wind-wave growth," *J. Geophys. Res.* **114**, C07012, doi:10.1029/2008JC005238 (2009).
- <sup>23</sup>T. Hara, E. J. Bock, and D. Lyzenga, "*In situ* measurements of capillary-gravity wave spectra using a scanning laser slope gauge and microwave radars," *J. Geophys. Res.* **99**, 12593, doi:10.1029/94JC00531 (1994).
- <sup>24</sup>T. Hara, E. J. Bock, and M. Donelan, "Frequency-wavenumber spectrum of wind-generated gravity-capillary waves," *J. Geophys. Res.: Oceans* **102**, 1061, doi:10.1029/96JC03229 (1997).
- <sup>25</sup>E. J. Bock, and T. Hara, "Optical measurements of capillary-gravity wave spectra using a scanning laser slope gauge," *J. Atmos. Oceanic Technol.* **12**, 395 (1995).
- <sup>26</sup>P. A. Hwang, D. B. Trizna, and Jin Wu, "Spatial measurements of short wind waves using a scanning slope sensor," *Dyn. Atm. Oceans* **20**, 1 (1993).
- <sup>27</sup>C. Cox and W. Munk, "Measurement of the roughness of the sea surface from photographs of the Sun's glitter," *J. Opt. Soc. Am.* **44**, 838 (1954).
- <sup>28</sup>I. Grant, N. Stewart, and I. A. Padilla-Perez, "Topographical measurements of water waves using the projection moire method," *Appl. Opt.* **29**, 3981 (1990).
- <sup>29</sup>P. Atsavapranee, J. B. Carneal, C. W. Baumann, J. H. Hamilton, and J. A. Shan, NSWCCD-50-TR-2005/022, Naval Surface Warfare Center, Carderock Division, Bethesda, MD, 2005.
- <sup>30</sup>B. Jähne and K. S. Riemer, "Two-dimensional wave number spectra of small-scale water surface waves," *J. Geophys. Res.* **95**, 11531, doi:10.1029/JC095iC07p11531 (1990).
- <sup>31</sup>X. Zhang and C. S. Cox, "Measuring the two-dimensional structure of a wavy water surface optically: A surface gradient detector," *Exp. Fluids* **17**, 225 (1994).
- <sup>32</sup>X. Zhang, "Surface image velocimetry for measuring short wind wave kinematics," *Exp. Fluids* **35**, 653 (2003).
- <sup>33</sup>D. Kieffaber, S. Reith, R. Rocholz, and B. Jähne, "High-speed imaging of short wind waves by shape from refraction," *J. Eur. Opt. Soc.: Rapid Publ.* **9**, 14015 (2014).
- <sup>34</sup>A. Paquier, F. Moisy, and M. Rabaud, "Surface deformations and wave generation by wind blowing over a viscous liquid," *Phys. Fluids* **27**, 122103 (2015).
- <sup>35</sup>B. Jähne, M. Schmidt, and R. Rocholz, "Combined optical slope/height measurements of short wind waves: Principle and calibration," *Meas. Sci. Technol.* **16**, 1937 (2005).
- <sup>36</sup>L. J. Cote, J. O. Davis, W. Marks, R. J. McGough, E. Mehr, W. J. Pierson, J. F. Ropek, G. Stephenson, and R. C. Vetter, *Meteorological Papers* (NYU College of Engineering, 1960), Vol. 2, p. 1.
- <sup>37</sup>O. H. Shemdin, H. M. Tran, and S. C. Wu, "Directional measurement of short ocean waves with stereophotography," *J. Geophys. Res.* **93**, 13891, doi:10.1029/JC093iC11p13891 (1988).
- <sup>38</sup>M. L. Banner, I. S. F. Jones, and J. C. Trinder, "Wavenumber spectra of short gravity waves," *J. Fluid Mech.* **198**, 321 (1989).
- <sup>39</sup>J. M. Wanek and C. H. Wu, "Automated trinocular stereo imaging system for three-dimensional surface wave measurements," *Ocean Eng.* **33**, 723 (2006).
- <sup>40</sup>A. Benetazzo, "Measurements of short water waves using stereo matched image sequences," *Coastal Eng.* **53**, 1013 (2006).
- <sup>41</sup>A. Benetazzo, F. Fedele, G. Gallego, P.-C. Shih, and A. Yezzi, "Offshore stereo measurements of gravity waves," *Coastal Eng.* **64**, 127 (2012).
- <sup>42</sup>G. Gallego, A. Yezzi, F. Fedele, and A. Benetazzo, "A variational stereo method for the three-dimensional reconstruction of ocean waves," *IEEE Trans. Geosci. Remote Sens.* **49**, 4445 (2011).
- <sup>43</sup>M. V. Kosnik and V. A. Dulov, "Extraction of short wind wave spectra from stereo images of the sea surface," *Meas. Sci. Technol.* **22**, 015504 (2010).
- <sup>44</sup>F. Fedele, A. Benetazzo, G. Gallego, P.-C. Shih, A. Yezzi, F. Barbariol, and F. Ardhuin, "Space-time measurements of oceanic sea states," *Ocean Modell.* **70**, 103 (2013).
- <sup>45</sup>F. Leckler, F. Ardhuin, C. Peureux, A. Benetazzo, F. Bergamasco, and V. Dulov, "Analysis and interpretation of frequency-wavenumber spectra of young wind waves," *J. Phys. Oceanogr.* **45**, 2484 (2015).
- <sup>46</sup>A. Benetazzo, F. Barbariol, F. Bergamasco, A. Torsello, S. Carniel, and M. Sclavo, "Stereo wave imaging from moving vessels: Practical use and applications," *Coastal Eng.* **109**, 114 (2016).
- <sup>47</sup>D. Liberzon and L. Shemer, "Experimental study of the initial stages of wind waves' spatial evolution," *J. Fluid Mech.* **681**, 462 (2011).
- <sup>48</sup>P. A. Lange, B. Jähne, J. Tschiessch, and J. Ilmberger, "Comparison between an amplitude-measuring wire and a slope-measuring laser water wave gauge," *Rev. Sci. Instrum.* **53**, 651 (1982).
- <sup>49</sup>E. Sanker, M.Sc. thesis, Tel-Aviv University, 2012.
- <sup>50</sup>A. Zavadsky and L. Shemer, "Characterization of turbulent airflow over evolving water-waves in a wind-wave tank," *J. Geophys. Res.* **117**, C00J19, doi:10.1029/2011JC007790 (2012).
- <sup>51</sup>J. Y. Bouquet, Technical Report, CalTech, Pasadena, 2004, [www.vision.caltech.edu/bouquet/calib\\_doc/index.html](http://www.vision.caltech.edu/bouquet/calib_doc/index.html).
- <sup>52</sup>G. Gallego, A. Benetazzo, A. Yezzi, and F. Fedele, in *ASME 2008 27th International Conference on Offshore Mechanics and Arctic Engineering* (ASME, 2008), p. 801.
- <sup>53</sup>A. S. Mironov, M. V. Yurovskaya, V. A. Dulov, D. Hauser, and C.-A. Guérin, "Statistical characterization of short wind waves from stereo images of the sea surface," *J. Geophys. Res.* **117**, C007860, doi:10.1029/2011JC007860 (2012).
- <sup>54</sup>B. Jähne, *Spatio-Temporal Image Processing: Theory and Scientific Applications* (Springer Science and Business Media, 1993), Vol. 751.
- <sup>55</sup>J. J. Rodriguez and J. K. Aggarwal, "Matching aerial images to 3-D terrain maps," *IEEE Trans. Pattern Anal. Mach. Intell.* **12**, 1138 (1990).
- <sup>56</sup>A. Benetazzo, F. Barbariol, F. Bergamasco, A. Torsello, S. Carniel, and M. Sclavo, "Observation of extreme sea waves in a space-time ensemble," *J. Phys. Oceanogr.* **45**, 2261 (2015).
- <sup>57</sup>B. Jähne, J. Klinke, and S. Waas, "Imaging of short ocean wind waves: A critical theoretical review," *J. Opt. Soc. Am. A* **11**, 2197 (1994).
- <sup>58</sup>H. Nobach and M. Honkanen, "Two-dimensional Gaussian regression for sub-pixel displacement estimation in particle image velocimetry or particle position estimation in particle tracking velocimetry," *Exp. Fluids* **38**, 511 (2005).
- <sup>59</sup>P. Boccotti, *Wave Mechanics for Ocean Engineering*, Elsevier Oceanography Series (Oxford, UK, 2000).
- <sup>60</sup>G. Cailliez and F. Collard, "Three-dimensional evolution of wind waves from gravity-capillary to short gravity range," *Eur. J. Mech. B/Fluids* **18**, 389 (1999).
- <sup>61</sup>D. L. Fugal, *Conceptual Wavelets in Digital Signal Processing: An In-depth, Practical Approach for the Non-Mathematician* (Space and Signals Technologies LLC, 2009).
- <sup>62</sup>L. Shemer, "On the directly generated resonant standing waves in a rectangular tank," *J. Fluid Mech.* **217**, 143 (1990).